Exploiting mechanisms for hierarchical branching structure of lung airway

Running title: Hierarchical branching in lung

Hisako Takigawa-Imamura,[1,*] Katsumi Fumoto,[2] Hiroaki Takesue,[3, 4] and Takashi Miura [1]

[1]Anatomy and Cell Biology, Graduate School of Medical Sciences, Kyushu University, 3-1-1 Maidashi, Higashi-ku, Fukuoka 812-8582, Japan

[2]Department of Molecular Biology and Biochemistry, Graduate School of Medicine, Osaka University, 2-2 Yamadaoka, Suita, 565-0871, Japan

[3]Graduate School of Pharmaceutical Sciences, Kyushu University, 3-1-1 Maidashi, Higashi-ku, Fukuoka 812-8582, Japan

*Correspondence: imamura.hisako.024@m.kyushu-u.ac.jp

[4]Hiroaki Takesue's present address is Biochemistry, Graduate School of Medical Sciences, Kyushu University, 3-1-1 Maidashi, Higashi-ku, Fukuoka 812-8582, Japan.

Abstract

The lung airways exhibit distinct features with long, wide proximal branches and short, thin distal branches, crucial for optimal respiratory function. In this study, we investigated the mechanism behind this hierarchical structure through experiments and modeling, focusing on the regulation of branch length and width during the pseudoglandular stage. To evaluate the response of mouse lung epithelium to fibroblast growth factor 10 (FGF10), we monitored the activity of extracellular signal-regulated kinase (ERK). ERK activity exhibited an increase dependent on the curvature of the epithelial tissue, which gradually decreased with the progression of development. We then constructed a computational model that incorporates curvature-dependent growth to predict its impact on branch formation. It was demonstrated that branch length is determined by the curvature dependence of growth. Next, in exploring branch width regulation, we considered the effect of apical contraction, a mechanism we had previously proposed to be regulated by Wnt signaling. Analysis of a mathematical model representing apical constriction showed that branch width is determined by cell shape. Finally, we constructed an integrated computational model that includes curvature-

dependent growth and cell shape controls, confirming their coordination in regulating branch formation. This study proposed that changes in the autonomous property of the epithelium may be responsible for the progressive branch morphology.

Introduction

Mammalian lung airways exhibit an intricate tree-like structure that contributes to the efficiency of respiratory function. The lung airways are formed by repetitive elongation and bifurcation of the epithelial tube, which is common in organs such as blood vessels, kidneys, and glandular organs. The architecture of major airways (such as the main bronchi, lobar bronchi, and segmental bronchi) shows a stereotyped pattern in humans [1–3], suggesting the existence of a mechanism to program the large-scale design. In mouse lungs, early-formed proximal branch segments are thick and long; in contrast, distal branch segments become thinner and shorter [4–6]. Unlike the botanical tree, in which new branches are always thin, the lumen size of the lung epithelial tip is large in the early stage and decreases as bifurcation proceeds. In addition, branching events occur more frequently as development progresses [4,7–9], suggesting that branch formation is

53 controlled with the developmental phase to configure the hierarchical structure. Several
54 biological and theoretical investigations have explored the principle of epithelial
55 branching through epithelial-mesenchymal interaction [10–16], but little is known about
56 how the macroscopic configuration is ordered. In this study, we aimed to address the
57 regulation of changes in the branch diameter and segment length during lung development.

58 Epithelial-mesenchymal interaction is mediated by diffusible molecules such as
59 fibroblast growth factor (FGF), bone morphogenic protein (BMP), sonic hedgehog (Shh),
60 and Wnt [17,18]. Signaling molecules control the spatiotemporal coordination of cellular
61 proliferation, migration, differentiation, and shape, leading to the arrangement of various
62 cells in the prescribed shape for tissue formation. During lung development, epithelial
63 growth is mainly promoted by FGF10, which is expressed in the outermost boundary of
64 the mesenchyme [11,19,20]. FGF10 also induces epithelial expression of Shh, which
65 diffuses into the mesenchyme and adversely represses FGF10 expression [21,22].
66 Theoretical studies have shown that this feedback interaction leads to interfacial
67 instability in the growing epithelium and promotes epithelial branching [23]. This is
68 similar to the mechanism by which bacterial colonies grow under nutrient-deprived

69 conditions, where regions of high curvature are exposed to residual nutrients and elongate
70 faster than regions of low curvature [24,25]. The tendency of the tip to grow faster is a
71 common mechanism for spontaneous branch formation, such as crystal growth and
72 viscous fingering [26–28]. Branching and bud formation with patterned proliferative
73 activity at branch tips have also been observed for epithelial explants in extracellular
74 matrix gels with an unbiased FGF distribution [10]. Drawing from these experimental
75 insights, the diffusion-limited growth of epithelium has been described using reaction-
76 diffusion [13,29] or phase-field schemes [12,30]. The mechanism of how heterogeneity
77 of growth activity emerges is unknown; thus, the profile of FGF signaling activity in the
78 lung epithelium requires confirmation to verify the common concept of branch formation
79 models.

80 Wnt is also crucial for lung development [18]. The Wnt/ β-catenin pathway mediates
81 cell fate determination in the embryonic state. In the lung mesenchyme, Wnt2 and Wnt2b
82 are expressed as master regulators of proximal and distal patterning, which are
83 distinguished by the epithelial expression of SOX2 and SOX9, respectively [31,32]. Loss
84 of Wnt2/2b expression results in lung hypoplasia in the absence of small distal branches

85 [33,34]. Double mutation of transcription factors Tbx2 and Tbx3, which act downstream
86 of Shh and upstream of Wnt, respectively, also severely reduces the number of distal tips
87 by inhibiting mesenchymal proliferation [35]. These findings indicate that Wnt may
88 contribute to the generation of distal branches in the lungs. We previously reported that
89 Wnt switches epithelial development from the branching phase (called the
90 pseudoglandular stage) to the alveolus-shaping phase (canalicular stage), emphasizing the
91 importance of Wnt signaling in distal duct morphology [36]. It was also revealed that
92 activation of the Wnt/β-catenin pathway induces apical constriction of the lung
93 epithelium and eventually scales down the bud size that emerges in mesenchyme-free
94 epithelial cyst culture. Bud formation is an *in vitro* model of branch formation; therefore,
95 our results indicate that Wnt signaling assists FGF10 in branching events. These results
96 are consistent with a previous report showing that deletion of the Wnt receptor Fzd2
97 causes branching defects and cystic lung *in vivo* [37]. In this study, we considered how
98 the interplay of growth control by FGF10 and cell shape regulation by Wnt can adjust the
99 branch scale.

100 There are two distinct modes of lung branching: tip splitting and lateral branching

101 [4]. The former is the symmetrical bifurcation at the distal end of a growing branch, and
102 the latter is the sprouting in the middle of a branch. Stepwise observation of mouse lung
103 development revealed that lateral branching mainly occurs during the early phase in the
104 pseudoglandular stage, suggesting that lateral branching mainly generates asymmetric
105 major branches. In contrast, tip splitting sequentially occurs in different sizes and
106 frequencies during branch elongation, suggesting that the regulation of tip splitting is
107 crucial for the hierarchical structure of branches. Accordingly, we focused on tip splitting
108 in the pseudoglandular stage.

109 This study aimed to explore how branch formation is regulated in the lung through
110 experimental and theoretical examinations. Experimental verification of the protrusion-
111 grows-faster concept in the lung epithelium provides new insights into the tip-splitting
112 branching frequency change across developmental stages through FGF. We also observed
113 the change in cell size across the stages to explain the difference in tube size.
114 Mathematical models demonstrate how these observed properties contribute to the
115 hierarchical structure of the airways. Furthermore, we propose that apical constriction can
116 efficiently promote tip splitting of thin branches to regulate their length based on

observation of cell shape changes and mathematical analysis.

Materials and Methods

Animal

Transgenic mice expressing ERK FRET biosensors [38] were kindly provided by Michiyuki Matsuda (Kyoto University, Kyoto, Japan) through the JCRB Laboratory Animal Resource Bank of the National Institute of Biomedical Innovation. ERK FRET biosensors, EKAREV-nuclear export signals, are localized in the cytoplasm. ICR mice (Japan Charles River, Yokohama, Japan) were crossed with EKAREV mice, and the embryos were used for ERK activity measurement. ICR embryos were used for FGF10 uptake assay and immunostaining. All procedures involving animal experiments were reviewed and approved by the Ethics Committee of Animal Experiments, Kyushu University Graduate School of Medical Sciences (A25-182, A27-071, and A29-036).

Mesenchyme-free culture of embryonic lung epithelium in Matrigel

Embryonic mouse lungs (E12.5, E13.5, and E14.5) were dissected and washed with

133 Hank's balanced salt solution (HBSS). Lung lobes were cut into pieces and soaked in
134 dispase solution (1 U/mL in HBSS; Gibco) for 10 min at 37 °C. The tissues were washed
135 twice in 10 mL of HBSS. Repetitive pipetting of tissues in HBSS broke up the
136 mesenchyme and small epithelial explants remained. The supernatant containing
137 mesenchymal cells was removed using a Cell Strainer with 40-μm pores (Falcon). The
138 epithelial explants were picked using a micropipette under a stereomicroscope and placed
139 on the bottom of a 35-mm glass-bottomed dish (IWAKI, blanched explants) or the μ-Slide
140 Angiogenesis slide (*ibidi*, small explants for FGF10 dose-dependent assay). Matrigel
141 (Corning, No. 356237) containing recombinant human FGF10 protein (PeproTech) was
142 overlaid on explants and allowed to solidify for 15 min at 37°C, followed by the addition
143 of the medium (2 mL for 35-mm dishes, and 50 μm for a well of the angiogenesis slide).
144 The tissue culture medium was DMEM/Ham's F-12 (Nacalai Tesque) supplied with
145 Penicillin-Streptomycin Mixed Solution (×10, Nacalai Tesque), L-glutamine (584
146 mg/mL), and bovine serum albumin (10%). Samples were incubated for 18 h before ERK
147 activity measurement. The FGF10 concentration is indicated as the mass concentration in
148 the volume of the gel and medium.

149

150 **Quantification of ERK activity**

151 We used a 405 nm laser for excitation and acquired the 475 nm and 530 nm emissions
152 as CFP and YFP signals, respectively. The acquired confocal images were analyzed using
153 Fiji software (National Institute for Health). Local ERK activity was estimated as the ratio
154 of the YFP signal to the CFP signal in a small region of interest (ROI) with a diameter
155 defined based on epithelium thickness (Fig 1 and S1). The ROI was limited in the regions
156 where the signal of the epithelial cross section was acquired in the confocal image (123
157 ROIs for E12.5, 108 ROIs for E13.5, and 77 ROIs for E14.5, Fig 2 and S1). Mean
158 command in Fiji was used to reduce the effect of spatial noise before quantifying
159 fluorescence intensity, and signal ratios were corrected for background signal. Next, 2D
160 tissue curvature was calculated from a series of ROI canters. Curvature was calculated
161 from the coordinates of three ROIs four apart along adjacent data points to capture the
162 smooth tissue curvature. The 3D curvature was not successful because of tissue damage
163 caused by prolonged image acquisition times. The correlation with linear regression
164 between ERK activity averaged over five neighboring points and tissue curvature was

165 calculated by using *Mathematica* (Wolfram Research, Inc.).

166 The ERK activity of the cyst (Fig 2A and panel A in Fig S2) was calculated as the
167 ratio between the total intensities of YFP and CFP in the epithelial cyst area, excluding
168 the luminal area in the cross-section. The FGF10 dose dependency was estimated by
169 linear regression analysis, and its significant difference by developmental stage was tested
170 using two-way analysis of variance (ANOVA) in the statistical software R (R Core Team).

171

172 **FGF10 incorporation assay**

173 Recombinant FGF10 protein was labeled using an Alexa Fluor 488 Microscale
174 Protein Labeling Kit (Invitrogen). To reduce the loss of physiological activity of FGF10,
175 we optimized the labeling protocol and reduced the amount of Alexa Fluor used. The
176 labeling reaction was conducted by mixing 100 μL of FGF10 solution (1 μg/mL in
177 phosphate-buffered saline, PBS, pH 7.4), 5 μL of sodium bicarbonate (1 M), and 9.8 μL
178 of Alexa488 solution (1:10 diluted) at 22°C. After a 15-min reaction, the unreacted dye
179 in the sample was removed using a Slide-A-Lyser Mini Dialysis Unit (Thermo Scientific)
180 in PBS for 16 h at 4°C. The purified solution was collected, and the protein concentration

181 was measured using a NanoDrop spectrophotometer (Thermo Fisher). The FGF10-
182 Alexa488 solution was stored in small aliquots at -20°C to avoid freeze-thaw cycles.
183 Incubation and storage were performed in the dark.

184 Epithelial explants were embedded in Matrigel containing FGF10-Alexa488 protein
185 in a 35-mm dish, which was subsequently filled with the medium. The protein
186 incorporation was allowed for 3 h in a stage-top chamber (Tokai Hit) to maintain a 5%
187 CO_2-controlled atmosphere at 37°C followed by observation. The relative uptake activity
188 was measured as the mean fluorescent intensity in the epithelial area of the cross-section
189 of each explant. ROIs were defined as the round epithelial area, excluding the luminal
190 area in the cross-section. While epithelial explants from E14.5 formed cysts within 3
191 hours, those from E13.5 exhibited slower cyst formation, with most regions of interest
192 (ROIs) observed in sections from the tip regions (panel B in Fig S2).

193 FGF10 uptake was quantified as the mean intensity in the epithelial cyst area,
194 excluding the luminal area in the cross-section. The FGF10 dose dependency was
195 estimated by linear regression analysis, and its significant difference by developmental
196 stage was tested using two-way ANOVA in the statistical software R.
197

198 **Immunostaining and quantification of epithelial thickness**

199 Embryonic lungs from ICR mice were washed with PBS and fixed with methanol for
200 30 min. Permeabilization was in 0.1% Triton X-100 for 30 min, followed by the blocking
201 with 1.5% normal goat serum for 60 min. The samples were stained with anti-mouse E-
202 cadherin monoclonal antibody ECCD-2 (1:100, Takara) for 16 h at 4°C, followed by
203 washing three times with 0.1% Triton X-100 in PBS. After incubation with Alexa Fluor
204 488-conjugated goat anti-rat IgG secondary antibody (1:200, Thermo Fisher) for 30 min,
205 the sample was soaked in Sca*l*e reagent for tissue clearing overnight [39]. The cell nuclei
206 were stained with 5 μg/mL propidium iodide (PI; Dojindo).

207 Thickness measurement was conducted by drawing small circles with diameters
208 corresponding to the local thickness of the epithelium on the E-cadherin antibody-stained
209 images. Circles were positioned to overlap halfway along the epithelium. The diameters
210 of the circles were measured using Fiji and the mean and standard deviation were
211 calculated to represent the epithelial thickness for each sample. The ROIs designated for
212 thickness measurements are shown in Fig S3.

213

214 **Microscope observation**

215 The lung explants were observed at 20× magnification using a Nikon C1 confocal
216 microscope (Nikon Intech). Samples of live explants were kept in a stage-top chamber
217 (Tokai Hit) to maintain a 5% CO_2-controlled atmosphere at 37°C for cellular homeostasis
218 during the observation.

219

220 **Particle cell model of the curvature-dependent growth**

221 Particle-based two-dimensional (2D) model framework from our previous studies
222 was inspired by particle-based methods for fluid simulation, incorporating interactions
223 with Lennard-Jones-like potentials between particles [40–44]. In this study, the modeling
224 framework was employed to describe epithelial growth and deformation. Each particle
225 represents a cell (Fig 3). The cell-cell interaction and bending rigidity were introduced as
226 previously described [42,43]. Curvature-dependent tissue growth was newly incorporated
227 for this study and is mentioned in the Result section. Cell division event was described
228 by replacing a cell with two daughter cells with a radius of 0.2, which gradually grew to
229 the default mother cell radius of 0.4 in 1000 timesteps. Parameter values are in the

supplementary table (S1 Table).

To obtain the initial geometry, 50 cells were arranged in a U-shape with a width of 5. The ten leftmost cells were pinned in their initial position. For relaxation of the shape of the cell sequence, cells were not grown, and the cell sequence was smoothed by bending rigidity until the shape became stationary. After sufficient relaxation time, numerical calculations of growth were performed. Pinned cells were not allowed to grow through the calculation, while growth was assumed for the remaining right tip side.

The time development of the model was calculated using C++ with $\Delta t = 0.005$, and the graphics were generated using *Mathematica*. These computational procedures were used for other models throughout the study.

Quadrilateral cell model with apical constriction

To describe tissue deformation coupled with cell shape control, we applied the model framework in our previous studies [36,45], where the cell shape is represented by four vertices ($\boldsymbol{a}_i$, $\boldsymbol{a}_{i+1}$, $\boldsymbol{b}_i$, and $\boldsymbol{b}_{i+1}$ in Fig 4A) and the displacement of vertices are calculated. Three attributes are considered for cell shape: apical length, basal length, and cell area,

each with its respective target value. A harmonic potential W and force $\boldsymbol{f}$ associated with the vertex $\mathbf{x}$ can be considered as follows:

$$W = \frac{1}{2}\left(\bar{u} - u(\boldsymbol{x})\right)^2, \quad \boldsymbol{f} = -\frac{\partial W}{\partial \boldsymbol{x}}, \qquad (1)$$

where $u(\boldsymbol{x})$ is an attribute value and, $\bar{u}$ is its corresponding target value. The forces for each attribute were calculated by Eq (1). The target value of apical length is 0 for introducing apical constriction (Fig 4B). It was assumed that all cells exhibit uniform apical contraction for simplicity. The area regulation force based on isotropic restoration [36] tended to destabilize the cell shape, thus it was simplified to be based on adjusting the lateral length as follows:

$$\boldsymbol{f}_i^{\mathrm{sa}} = k_{\mathrm{s}}(2\bar{s} - s_{i-1} - s_i)\frac{\boldsymbol{a}_i - \boldsymbol{b}_i}{|\boldsymbol{a}_i - \boldsymbol{b}_i|}, \qquad (2)$$

$$\boldsymbol{f}_i^{\mathrm{sb}} = k_{\mathrm{s}}(2\bar{s} - s_{i-1} - s_i)\frac{\boldsymbol{b}_i - \boldsymbol{a}_i}{|\boldsymbol{b}_i - \boldsymbol{a}_i|}. \qquad (3)$$

Eqs (2) and (3) are for the apical vertex $\boldsymbol{a}_i$ and the basal vertex $\boldsymbol{b}_i$, respectively. The

coefficient k_s determines the magnitude of the regulation, s_i is the area formed by $\boldsymbol{a}_i$, $\boldsymbol{a}_{i\text{-}1}$, $\boldsymbol{b}_{i\text{-}1}$, and $\boldsymbol{b}_i$, and $\bar{s}$ is its target value. When the two cells sharing the vertex are symmetrical in shape, Eqs (2) and (3) are consistent with the energy-derived force [36].

To realize stable natural tissue shape, cell shape symmetry regulation was assumed for each cell, and bending rigidity was assumed for the sequence of the basal vertex as detailed previously [36]. Parameter values were adjusted for this study (S2 Table). We considered the displacement of the cell in the viscosity-dominated regime as follows:

$$\boldsymbol{x}_i^{t+\Delta t} = \boldsymbol{x}_i^t + \gamma^{-1}\boldsymbol{f}_i\Delta t\,, \quad (4)$$

where $\boldsymbol{x}_i$ is a non-dimensionalized position vector of the i-th cell center, γ is the friction coefficient, t is time, and $\Delta t = 0.005$ is the timestep size.

Cell migration and division were assumed to depend on tissue curvature. Cell division was described by inserting new vertices into the middle of the edges of a fully grown cell at a probability q_i. The daughter cells are set at half the size of the mother cells at the time of division and grow over 50,000 timesteps. Cell migration is described as the

outward movement of vertices on the basal side represented by $\boldsymbol{f}_i^{\mathrm{w}}$. The dependency on the tissue curvature was assumed as follows:

$$q_i = \begin{cases} k_{\mathrm{q}}(\varphi_i - \varphi_{\mathrm{q}}) + \bar{q} & \text{for } \varphi_i > \varphi_{\mathrm{q}} \\ 0 & \text{for } \varphi_i \leq \varphi_{\mathrm{q}} \end{cases}, \quad (5)$$

$$\boldsymbol{f}_i^{\mathrm{w}} = \begin{cases} k_{\mathrm{w}} \varphi_i \boldsymbol{n}_{i-3,i+3} & \text{for } \varphi_i > \varphi_{\mathrm{w}} \\ 0 & \text{for } \varphi_i \leq \varphi_{\mathrm{w}} \end{cases}, \quad (6)$$

$$\varphi_i = \pi - \angle \boldsymbol{b}_{i-3} \boldsymbol{b}_i \boldsymbol{b}_{i+3}, \quad (7)$$

where k_{w} and k_{q} are the strength of curvature dependence, $\boldsymbol{n}_{i,j}$ is the normal vector to $\boldsymbol{x}_i$-$\boldsymbol{x}_j$, φ_{w} and φ_{q} are the critical angles for migration and cell division, and $\bar{q}$ is the basic probability of cell division. Tissue curvature was approximated using φ_i as an alternative to θ_i, aiming to avoid detecting local distortions.

The initial shape in Fig 4C and 4D was a thin tubular shape with an outer width of 3. The three leftmost vertices were pinned at the initial positions. After sufficient relaxation time, numerical calculations of growth were performed. Cells with pinned vertices were not allowed to grow through the calculation, while growth was assumed for the remaining right tip side.

In Fig 5A, epithelial cysts were depicted. No vertices were pinned, and no growth was assumed. Initially, $k_a = 0$ was set and increased by 0.003 at each timestep until $k_a = 3$.

Estimating mechanical instability in the cyst models

In the quadrilateral cell model, cysts were depicted in Fig 5A. Potential energy calculations were performed for these representations (Fig 5B–E), ranging from circular to elongated shapes, by considering the combination of a rectangle of length x and a semicircle of radius y. The longitudinal length of the cyst is $L = x + 2y$. It was assumed that the basal length and cell area are uniformly maintained as $\bar{b}$ and $\bar{s}$, respectively. The sum of the basal lengths in the cyst is $\bar{b}n = 2x + 2\pi y$. The apical lumen was approximated as an ellipse with a major radius α and a minor radius β. We estimated α and β by considering the conservation of cell areas and the relationship between cell height and apical length. The apical length of the cell with the highest curvature is denoted by a_y. We assumed $a_y/\alpha = \bar{b}/(x/2 + y)$ by considering the cell shape as a trapezoid. The area of the cell is given by $\bar{s} = (a_y + \bar{b})(y + x/2 - \alpha)/2$, where α was derived as

in Eq (8) below. Additionally, given that the elongated cyst area is equal to the circular cyst area, expressed as $n\bar{s} = 2xy + \pi y^2 - \pi\alpha\beta$, β was derived as in Eq (9). Eqs (8) and (9) are as follows:

$$\alpha = \frac{1}{2}\sqrt{L^2 - 4\bar{s}/\bar{b}}\,, \quad (8)$$

$$\beta = \frac{\left(\bar{b}n - 2L\right)\left((\pi - 4)\bar{b}n + 2L\pi\right)}{4\pi\alpha(\pi - 2)^2} - \frac{\bar{s}}{\alpha}\,. \quad (9)$$

Cell type switching model

The model dynamics of integrated (Fig 6) is based on the quadrilateral cell model, with parameter values provided in the supplementary table (Table S3). The cell is initially of the tip type and switches to the duct type when $\varphi_i > \varphi_{\mathrm{d}}$. The regulation of apical length and cell area were assigned for the tip type (k_{at}, $\bar{a}_{\mathrm{t}}$, and $\bar{s}_{\mathrm{t}}$) and duct type (k_{ad}, $\bar{a}_{\mathrm{d}}$, and $\bar{s}_{\mathrm{d}}$), respectively. The triangle-like shape of the tip type was described by setting the optimal apical length $\bar{a}_{\mathrm{t}} = 0$. The tall columnar shape of the duct type was characterized by setting $\bar{s}_{\mathrm{t}} < \bar{s}_{\mathrm{d}}$ for the optimal cell area and equalizing apical and basal lengths as $\bar{a}_{\mathrm{d}} = \bar{b}$. Migration was assumed only for the duct type and described by moving the basal

326 vertex with force $\boldsymbol{f}_i^{\mu} = k_{\mu}\boldsymbol{n}_{i-3,i+3}$. The difference in the epithelial thickness was

327 described by changing $\bar{b}$.

328 The initial shape was assumed to be the tip of an epithelial branch with a width of 10,

329 in which 13 cells at the tip were assumed to be the tip type and the others were assumed

330 to be the duct type. Cells at the proximal ends were pinned at their initial positions and

331 no cell division was assumed in these cells.

332

333 Results

334 Verification of the enhanced FGF10 signaling in protruded regions of lung 335 epithelium

336 The assumption that the protruded region of the epithelium shows high growth

337 activity is commonly required in theoretical models to reproduce branching patterns [12–

338 14,46]. We examined extracellular signal-regulated kinase (ERK) activity as a hallmark

339 of FGF receptor 2 (FGFR2) activation in embryonic mouse lungs (Fig 1 and S1). Lung

340 explants from a transgenic mouse strain expressing a fluorescence resonance energy

341 transfer (FRET) biosensor for ERK activity were used [38]. To facilitate the laser light

342 for FRET detection in the epithelium, we used a mesenchyme-free epithelium culture
343 supplemented with recombinant FGF10 protein. Fig 1 shows the ERK activity map in the
344 epithelium of the mouse lung at embryonic day 12.5 (E12.5), E13.5, and E14.5, which
345 are the early pseudoglandular stage. It was demonstrated that ERK activity correlates with
346 the cross-sectional curvature of the epithelial explants as $R^2 = 0.41$ in E12.5 and $R^2 = 0.45$
347 in E13.5, suggesting that FGF10 signaling was enhanced in protruded regions (Fig 1A
348 and 1B). However, poor correlation and activation were observed in the E14.5 epithelium
349 as $R^2 = 0.0031$ (Fig 1C). This result also excluded the possibility that the higher FRET
350 signals at the protruded regions of the earlier explants were not due to differences in
351 detection efficiency. The linear regression analysis revealed a progressive decline in the
352 signal-to-curvature relationship, with a slope of 6.18 at E12.5, 2.93 at E13.5, and 0.12 at
353 E14.5. These results revealed that the signaling response of the epithelium to FGF10 is
354 gradually attenuated with development, indicating the modification of epithelial
355 properties during the developmental process.

356 We further examined whether the difference in ERK activity reflected its sensitivity
357 to FGF10 concentration (Fig 2). Small explants (<100 μm) of the distal epithelium were

358 grown in Matrigel with various concentrations of FGF10 for 18 h, and the ERK activity
359 of each cyst was measured (panel A in Fig S2). It was demonstrated that FGF10 enhanced
360 ERK activity in a dose-dependent manner, with a correlation of $R^2 = 0.53$ (Fig 2A, black
361 dots). E14.5 cysts showed a poor correlation with $R^2 = 0.013$ (Fig 2A, blue dots), which
362 is consistent with Fig 1C. The slope of regression lines in E13.5 was significantly larger
363 than in E14.5, with $P = 0.0014$, whereas the significant differences in intercepts were
364 rejected, suggesting a higher dose dependency in E13.5 than in E14.5. ERK activation
365 levels vary among cysts for the same FGF10 concentration and the same developmental
366 stage, indicating that epithelial segments may have intrinsic FGF signaling reactivity.

367 These variations in ERK activity may be due to differences in FGF10-FGFR2
368 interaction. It was reported that FGF10 stimulates the internalization of FGFR2 as early
369 endosomes [47]. Thus, we visualized FGF10 uptake into cells to observe receptor
370 activation (Fig 2B). Epithelial explants were cultured with fluorescence-labeled FGF10
371 (FGF10-Alexa488) for 3 h, resulting in the appearance of small fluorescent particles
372 inside the cells (panel B in Fig S2). Immunohistological analysis showed that FGF10 and
373 FGFR2 localization overlapped with the fluorescent signals, suggesting that the signals

374 reflected FGF10-Alexa488 uptake into cells by FGFR2 internalization (Fig S4). Unlike
375 ERK activity, tissue curvature dependency of FGF10 uptake was not detected. The
376 average fluorescent intensity of the explants showed a correlation with the FGF10 dose
377 in E13.5 (R^2 = 0.87) and E14.5 (R^2 = 0.72), with slopes of 20.7 and 9.7, respectively (Fig
378 2B). These regression lines differed significantly with $P = 1.2 \times 10^{-7}$. Collectively, these
379 results suggest that epithelial responsiveness to FGF10 declines with the developmental
380 stages in the lung epithelium, resulting in a difference in the activity gradient depending
381 on the tissue curvature.
382
383 **Modeling the curvature-dependent epithelial growth**
384 We considered that epithelial responsiveness to FGF10 may affect the branching
385 pattern and examined this by constructing a mathematical model. The longitudinal section
386 shape of the epithelial duct was described in a 2D space by adopting a model framework,
387 which we tentatively call the particle cell model, in which cells were assumed to be
388 interacting particles [40–44]. We aimed to represent the curvature-dependent growth
389 process of the tissue in the simplest form, in which the FGF10 distribution was omitted.

The cell was assumed to be a uniform circular shape, forming a chain of cells (Fig 3A). Distance-dependent interaction was assumed so that the cells bind to neighboring cells at a fixed distance, as described previously [42,43]. The bending rigidity along the sequence of cells was introduced to express the smooth contours of the tissue as described [42,43]. The interaction strength and bending rigidity are controlled by parameters k_{wall} and k_{bend}, respectively.

Tissue growth was incorporated so that the protruded regions grew faster. Cell migration and division were assumed to depend on local tissue curvature as a phenomenological simplification of epithelial diffusion-limited growth. The local tissue angle θ_i was used instead of calculating the local curvature (Fig 3B). The probability p_i that the i-th cell divides in each timestep is as follows:

$$p_i = \begin{cases} k_{\mathrm{p}}(\theta_i - \theta_{\mathrm{p}}) + \hat{p} & \text{for } \theta_i > \theta_{\mathrm{p}} \\ 0 & \text{for } \theta_i \leq \theta_{\mathrm{p}} \end{cases}, \quad (10)$$

$$\theta_i = \pi - \angle \boldsymbol{x}_{i-1}\boldsymbol{x}_i\boldsymbol{x}_{i+1}, \quad (11)$$

where k_{p} is associated with the angle dependence, θ_{p} is the minimum angle for the cell

division, $\hat{p}$ is the basic probability, and $\boldsymbol{x}_i$ designates the i-th cell position. FGF10 is also known to be involved in the regulation of cell migration [10,19,48]. Here we assumed simple outward movement as follows:

$$\boldsymbol{f}_i^{\mathrm{m}} = \begin{cases} k_{\mathrm{m}}(\theta_i)^2 \boldsymbol{n}_{i-1,i+1} & \text{for } \theta_i > 0 \\ 0 & \text{for } \theta_i \leq 0 \end{cases}, \quad (12)$$

where $\boldsymbol{f}_i^{\mathrm{m}}$ represents the active migration in the normal direction of the tissue, and k_{m} is the coefficient.

The cell position changes according to the sum of the calculated forces of the cell-cell interaction, bending rigidity, and migration. The initial shape for the model simulation was assumed to be the tip of the epithelial branch (Fig 3C, left-most image). The cells at the proximal ends were pinned in their initial positions and the distal tip was grown according to curvature-dependent growth, thus depicting the successive tip-splitting deformation (Fig 3C). We further examined how the curvature dependency, denoted by k_{m} and k_{p}, affects branch shape (Fig 3D). It was revealed that larger k_{m} and k_{p} values resulted in a longer segment length, suggesting that epithelial responsiveness

422 determines the segment length during airway construction. When the curvature
423 dependency was high, extremely restricted tip growth facilitates tip elongation instead of
424 tip splitting. In contrast, in the case of low dependency, broad growth causes tip curvature
425 reduction, causing shape instability. However, the branch width did not show significant
426 differences among the cases with different curvature dependencies, and the entire
427 mechanism of the hierarchy construction could not be explained by the responsiveness
428 change.
429
430 **Modeling branch formation with cell shape regulation**
431 To explore the control mechanism of tube size, we focused on the role of cell shape
432 regulation. We have reported that the lung epithelium exhibits apical constriction and
433 facilitates the formation of small buds through Wnt signaling [36]. Inhibition of Wnt
434 signaling has been demonstrated to impede the formation of distal fine branches and
435 induce cystic expansion in mice [31,33]. Drawing from these observations, we considered
436 that apical constriction may facilitate tip splitting to form distal fine branches. To explore
437 this hypothesis, we investigated the impact of apical constriction on branch shape (Fig 4).

438 We employed the model established in previous studies [36,45], where each cell is
439 represented as a quadrilateral (Fig 4A) to incorporate apical constriction. The model
440 framework is based on the harmonic potential control of each edge length and area, and
441 apical constriction was implemented by applying an attractive force between the pair of
442 apical vertices (Fig 4B). In this study, we extended the model by incorporating curvature-
443 dependent growth. It was confirmed that curvature-dependent growth promoted branch
444 elongation when no apical constriction was assumed (Fig 4C). When apical constriction
445 was assumed, tip splitting was induced (Fig 4D). Apical constriction facilitates tip
446 splitting due to mechanical instability caused by the imbalance between the increase in
447 cell-autonomous curvature due to apical constriction and the decrease in tissue curvature
448 due to growth [15,36,49].

449 To understand the model dynamics and to explore the mechanisms governing branch
450 width, we depicted small cysts consisting of 13–18 cells and examined the impact of
451 apical constriction (Fig 5). It was demonstrated that apical constriction transformed the
452 cyst from a circular shape to an elongated shape if the cyst contained more than 15 cells;
453 otherwise, the cyst sustained a circular shape (Fig 5A).

Next, we analyzed how the number of cells in the cyst influence the transition from a circular cyst to an elongated shape. The potential energy of the circular state E_c and that of the elongated state E_e were compared (Fig 5B). The longitudinal cyst length, designated by L, serves as a defining parameter for the cyst shape. The potential energy of the cyst was assessed based on the regulation of basal length, apical length, and cell area. When it was assumed the basal length and area are sustained by strong regulation, E_c-E_e is derived from the sum of apical lengths as follows:

$$E_c - E_e = \sum_i^n k_\mathrm{a} c_i - \sum_i^n k_\mathrm{a} e_i \ , \qquad (13)$$

where n is the cell number, k_a represents the strength of apical constriction [36,45], and c_i and e_i are the apical lengths of the i-th cell in the circular and elongated cysts, respectively. The sums of the apical lengths were approximated as circular and elliptic circumferences of the cyst lumen as follows:

$$\sum_i^n c_i \sim \sqrt{n^2 \bar{b}^2 - 4\pi n \bar{s}} \ , \qquad (14)$$

$$\sum_{i}^{n} e_i \sim \int_0^{2\pi} \sqrt{\alpha^2 - (\alpha^2 - \beta^2)\sin^2 x}\, dx\,, \quad (15)$$

where $\bar{b}$ and $\bar{s}$ are the basal length and area of the cell, $\alpha = L$ and β are the major and minor radius of an ellipse, respectively. The values of α and β can be estimated as the function of $\bar{b}$, $\bar{s}$, n, and L by considering the constant cell area.

Fig 5B shows the numerical profile of E_c-E_e against L for n ranging from 13 to 18. The condition $n > 12$ is required for $\bar{b} = \bar{s} = 1$, as $n^2\bar{b}^2 - 4\pi n\bar{s} > 0$ must be satisfied from Eq (14). The minimum L is $\bar{b}n/\pi$, which corresponds to a circular cyst. The maximum of E_c-E_e corresponds to the most stable shape, which is consistent with the model simulation (Fig 5A). The widths of the elongated cysts do not exceed the diameter of the smallest circular cyst, indicating that the same cell shape regulation condition induces spontaneous curvature (Fig 5C). In this regard, we obtained the minimum width among cysts with varying cell numbers and found its decrease with $\bar{b}/\bar{s}$, regardless of $\bar{s}$ (Fig 5D). This result suggested that cell height determines the spontaneous curvature, irrespective of cell size. Changes in cell size are compensated by alterations in cell number (Fig 5E) and do not affect the spontaneous curvature (Fig 5D).

486 Fig 5 revealed a correlation between epithelial thickness and branch width,
487 suggesting that the epithelium becomes thinner as development progresses. Supporting
488 this theoretical result, we observed the lung epithelium at E12.5, E13.5, and E14.5, noting
489 a progressive decrease in thickness to 70.3 ± 9.23 μm, 43.0 ± 9.66 μm, and 31.4 ± 4.08
490 μm, respectively (Fig 6). It should also be noted that E13.5 cysts *in vitro* showed the
491 tendency to be thicker during culture than the E14.5 cysts (Fig S5, black line in panel A
492 and blue solid line in panel C), indicating an intrinsic alteration in thickness regulation as
493 a developmental feature.

494 **Integrated modeling of curvature-dependent growth and cell shape regulation**

495 In addition to progressive changes in epithelial thickness, curvature-dependent
496 changes in epithelial thickness were also observed. The epithelium was thinner in the high
497 curvature tip region than in the low curvature duct (Fig 6 and 7A), consistent with the
498 detailed 3D analysis of cell shape in E11.5 mouse lung [37], suggesting distinct cell shape
499 regulation regimes for the tip and duct regions. Cells in the concave region were also
500 thickened (asterisks in Fig 7A), implying that the shift from tip-type cells to duct-type
501 cells is occurring during tip spitting event.

502 It has also been shown that canonical Wnt signaling is more intense in the tip region
503 of the lung epithelium [50,51]. We therefore constructed a model to represent that cells
504 in the tip region are highly active in growth and apical constriction.

505 The model framework is based on the quadrilateral cell model and two types of
506 epithelial cells were assumed: a short tip type exhibiting high growth activity and apical
507 constriction, and a tall duct type that lacks these activities (Fig 7B). The cell type is
508 determined depending on the angle formed by successive vertices, representative of local
509 curvature. The critical angle for switching φ_d determines the curvature dependency of
510 growth. The growth was described only for the tip type by migration represented by k_μ
511 and cell division with a constant probability ρ. In addition, distinct parameter values for
512 cell shape regulation were assigned to the tip and duct types, which are summarized in
513 S3 Table.

514 Fig 7C and 7D show that the integration of curvature-dependent growth and cell
515 shape change reproduced the higher-order branching process. Thicker epithelium with a
516 higher curvature dependency resulted in a larger-scale branching structure (Fig 7C),
517 compared to the case of thinner epithelium with a lower curvature dependency (Fig 7D).

Epithelial thickness and curvature dependence had an additive impact on branch scale (Fig 7C–E), suggesting that the changes in these epithelial features during development (Fig 1, 2, and 6) contribute to the progressive alteration in airway segment length. It was demonstrated that thin epithelium not only narrowed the branches (Fig 5) but also shortened the branches (Fig 7D and 7E), aligning with the progressive changes in epithelial thickness (Fig 6) and branch morphology [4]. Reduced apical constriction has a more significant effect on the tip shape in thin epithelium compared to thick epithelium (Fig 7F and 7G), consistent with Wnt signaling defects showing severe cystic morphology in the distal airway [33–35].

Discussion

We explored regulatory mechanisms to generate a hierarchical structure of the lung airways with a specific focus on epithelial properties. Our experimental observations revealed developmental changes in epithelium responsiveness to FGF10. Furthermore, by constructing a mathematical model assuming curvature-dependent growth, we demonstrated that such change leads to variations in branch segment length. Our analysis

534 also highlighted the involvement of cell height regulation in modulating branch width
535 through apical constriction. This study provides a new perspective on how epithelial
536 properties regulate the branching structure of the lung.

537 Morphogenesis is characterized by cells that are highly active and constantly
538 responding to various regulatory cues, making it an essentially intricate process.
539 Integrating such diverse behaviors into a model can complicate the pursuit of
540 comprehensive understanding. We narrowed down the cellular behaviors of interest based
541 on experimental observations in lung epithelial tissue. The agent-based approach enabled
542 us to explore the implications of curvature-dependent growth and cell shape control in
543 morphogenesis. Our models were based on experimental observations, while the
544 parameters of the model are not experimentally comparable and will need to be validated
545 in the future.

546 Theoretical studies on lung epithelial morphogenesis have been conducted based on
547 the FGF10 distribution, emphasizing the importance of signaling interaction between the
548 epithelium and mesenchyme [12,14,46]. However, it was later found that the expression
549 pattern of FGF10 in the lung mesenchyme is not required for epithelial branching [52],

550 triggering the hypothesis of an epithelium-autonomous morphogenetic mechanism
551 [15,16,36]. In line with this perspective, our computational models propose that the
552 branching structure of the lung is determined by epithelial properties, FGF10
553 responsiveness (Fig 3) and tissue thickness (Fig 5). The observation that early epithelia
554 exhibit higher growth activity (Fig 1 and 2), and thicker tissue (Fig 6) might be apparent
555 to biologists studying lung development. Additionally, we found that thinner epithelia are
556 more responsive to FGF10 (panel D in Fig S5), supporting the assumption that the tip
557 type cell is thinner and grows faster in the integrated model (Fig 7B). It was also revealed
558 that FGF10 exposure decreased cyst thickness (panels B and C in Fig S5), implying a
559 potential role of this essential signaling molecule for cell shape regulation.

560 The regulation of a specific growth activity at the epithelial protrusion remains an
561 unsolved issue (Fig 1). One potentially relevant mechanism is geometry-dependent
562 mechanical patterning [53]. When human embryonic stem cell-derived lung epithelial
563 progenitor cells were cultured inside the 100-μm tube, SOX2 expression was suppressed
564 via canonical Wnt signaling, whereas SOX9 expression was maintained [53]. The tissue
565 curvature-dependent regulation of SOX2 and SOX9 expression, which is regulated only

downstream of the Wnt/b-catenin pathway, is consistent with the assumption of curvature-dependent growth and apical contraction in our model (Fig 7). Clarifying how the cell shape and growth activity are regulated and how signaling pathways such as FGF and Wnt are involved is necessary to gain insight into the regulatory mechanisms of the global structure of the lung.

Author Contributions

H.T.-I. designed research, performed experimental and theoretical research, constructed models, and wrote the manuscript; H.T. executed experiments and analyzed data; K.F. and T.M. supervised research. All authors have read and approved the published manuscript.

Declaration of Interests

The authors declare no competing interests.

Acknowledgment

582 We thank Prof. Michiyuki Matsuda (Kyoto University) for the use of Eisuke
583 transgenic mice. We thank Ms. Yoshimi Yamaguchi for her technical assistance with the
584 FGF10 labeling experiment. This work was supported by JSPS KAKENHI Grant Number
585 18K06260 (H.T.-I.) and 15KT0018 (T.M).

586

587 # Reference

588 1. Boyden EA. The Nomenclature of the Bronchopulmonary Segments and Their
589 Blood Supply. Dis Chest. 1961;39: 1–6. doi:10.1378/chest.39.1.1
590 2. Jackson CL, Huber JF. Correlated Applied Anatomy of the Bronchial Tree and
591 Lungs With a System of Nomenclature. Dis Chest. 1943;9: 319–326.
592 doi:10.1378/chest.9.4.319
593 3. Fujii S, Muranaka T, Matsubayashi J, Yamada S, Yoneyama A, Takakuwa T.
594 Bronchial tree of the human embryo: Categorization of the branching mode as
595 monopodial and dipodial. PLoS One. 2021;16: 1–13.
596 doi:10.1371/journal.pone.0245558
597 4. Metzger RJ, Klein OD, Martin GR, Krasnow MA. The branching programme of
598 mouse lung development. Nature. 2008;453: 745–750. doi:10.1038/nature07005
599 5. Jones MR, Chong L, Bellusci S. Fgf10/Fgfr2b Signaling Orchestrates the
600 Symphony of Molecular, Cellular, and Physical Processes Required for
601 Harmonious Airway Branching Morphogenesis. Front Cell Dev Biol. 2021;8: 1–
602 24. doi:10.3389/fcell.2020.620667
603 6. Glenny RW, Krueger M, Bauer C, Beichel RR. The fractal geometry of bronchial
604 trees differs by strain in mice. J Appl Physiol. 2020;128: 362–367.
605 doi:10.1152/japplphysiol.00838.2019
606 7. Counter WB, Wang IQ, Farncombe TH, Labiris NR. Airway and pulmonary
607 vascular measurements using contrast-enhanced micro-CT in rodents. Am J
608 Physiol - Lung Cell Mol Physiol. 2013;304: 831–843.

609 doi:10.1152/ajplung.00281.2012
610 8. Tawhai MH, Hunter P, Tschirren J, Reinhardt J, McLennan G, Hoffman EA. CT-
611 based geometry analysis and finite element models of the human and ovine
612 bronchial tree. J Appl Physiol. 2004;97: 2310–2321.
613 doi:10.1152/japplphysiol.00520.2004
614 9. Nelson T, West B, Goldberger A. The fractal lung: Universal and species-related
615 scaling patterns. Experientia. 1990;46: 251–254.
616 10. Nogawa H, Morita K, Cardoso W V. Bud formation precedes the appearance of
617 differential cell proliferation during branching morphogenesis of mouse lung
618 epithelium in vitro. Dev Dyn. 1998;213: 228–235. doi:10.1002/(SICI)1097-
619 0177(199810)213:2<228::AID-AJA8>3.0.CO;2-I
620 11. Bellusci S, Grindley J, Emoto H, Itoh N, Hogan BLM. Fibroblast Growth Factor
621 10 (FGF10) and branching morphogenesis in the embryonic mouse lung.
622 Development. 1997;124: 4867–4878. doi:10.1242/dev.124.23.4867
623 12. Clément R, Blanc P, Mauroy B, Sapin V, Douady S. Shape Self-Regulation in
624 Early Lung Morphogenesis. Bellusci S, editor. PLoS One. 2012;7: e36925.
625 doi:10.1371/journal.pone.0036925
626 13. Miura T, Shiota K. Time-lapse observation of branching morphogenesis of the
627 lung bud epithelium in mesenchyme-free culture and its relationship with the
628 localization of actin filaments. Int J Dev Biol. 2000;44: 899–902.
629 14. Menshykau D, Kraemer C, Iber D. Branch mode selection during early lung
630 development. PLoS Comput Biol. 2012;8. doi:10.1371/journal.pcbi.1002377
631 15. Kim HY, Varner VD, Nelson CM. Apical constriction initiates new bud
632 formation during monopodial branching of the embryonic chicken lung. Dev.
633 2013;140: 3146–3155. doi:10.1242/dev.093682
634 16. Varner VD, Gleghorn JP, Miller E, Radisky DC, Nelson CM. Mechanically
635 patterning the embryonic airway epithelium. Proc Natl Acad Sci U S A.
636 2015;112: 9230–9235. doi:10.1073/pnas.1504102112
637 17. Iber D. The control of lung branching morphogenesis. Curr Top Dev Biol.
638 2021;143: 205–237. doi:10.1016/bs.ctdb.2021.02.002
639 18. Volckaert T, De Langhe SP. Wnt and FGF mediated epithelial-mesenchymal
640 crosstalk during lung development. Dev Dyn. 2015;244: 342–366.
641 doi:10.1002/dvdy.24234

642 19. Weaver M, Dunn NR, Hogan BLM. Bmp4 and Fgf10 play opposing roles during
643 lung bud morphogenesis. Development. 2000;127: 2695–2704.
644 doi:10.1242/dev.127.12.2695
645 20. Abler LL, Mansour SL, Sun X. Conditional gene inactivation reveals roles for
646 Fgf10 and Fgfr2 in establishing a normal pattern of epithelial branching in the
647 mouse lung. Dev Dyn. 2008;238: 1999–2013. doi:10.1002/dvdy.22032
648 21. Bellusci S, Furuta Y, Rush MG, Henderson R, Winnier G, Hogan BLM.
649 Involvement of Sonic hedgehog (Shh) in mouse embryonic lung growth and
650 morphogenesis. Development. 1997;124: 53–63. doi:10.1242/dev.124.1.53
651 22. Pepicelli C V., Lewis PM, McMahon AP. Sonic hedgehog regulates branching
652 morphogenesis in the mammalian lung. Curr Biol. 1998;8: 1083–1086.
653 doi:10.1016/S0960-9822(98)70446-4
654 23. Miura T, Shiota K. Depletion of FGF acts as a lateral inhibitory factor in lung
655 branching morphogenesis in vitro. Mech Dev. 2002;116: 29–38.
656 doi:10.1016/S0925-4773(02)00132-6
657 24. Matsushita M, Wakita J, Itoh H, Ràfols I, Matsuyama T, Sakaguchi H, et al.
658 Interface growth and pattern formation in bacterial colonies. Phys A Stat Mech
659 its Appl. 1998;249: 517–524. doi:10.1016/S0378-4371(97)00511-6
660 25. Ben-Jacob E, Shmueli H, Shochet O, Tenenbaum A. Adaptive self-organization
661 during growth of bacterial colonies. Phys A Stat Mech its Appl. 1992;187: 378–
662 424. doi:10.1016/0378-4371(92)90002-8
663 26. Daccord G, Nittmann J, Etienne S, Stanley HE. Radial viscous fingers and
664 diffusion-limited aggregation: Fractal dimension and growth sites. Phys Rev Lett.
665 1986;56: 336–339.
666 27. Yokoyama E, Kuroda T. Pattern formation in growth of snow crystals occurring
667 in the surface kinetic process and the diffusion process. Phys Rev A. 1990;41:
668 2038–2049. doi:10.1103/PhysRevA.41.2038
669 28. Lubkin SR, Murray JD. A mechanism for early branching in lung
670 morphogenesis. J Math Biol. 1995;34: 77–94. doi:10.1007/BF00180137
671 29. Hartmann D, Miura T. Modelling in vitro lung branching morphogenesis during
672 development. J Theor Biol. 2006;242: 862–872. doi:10.1016/j.jtbi.2006.05.009
673 30. George UZ, Bokka KK, Warburton D, Lubkin SR. Quantifying stretch and
674 secretion in the embryonic lung: Implications for morphogenesis. Mech Dev.

675 2015;138: 356–363. doi:10.1016/j.mod.2015.07.003
676 31. Mucenski ML, Wert SE, Nation JM, Loudy DE, Huelsken J, Birchmeier W, et al.
677 B-Catenin Is Required for Specification of Proximal/Distal Cell Fate During
678 Lung Morphogenesis. J Biol Chem. 2003;278: 40231–40238.
679 doi:10.1074/jbc.M305892200
680 32. Shu W, Guttentag S, Wang Z, Andl T, Ballard P, Lu MM, et al. Wnt/β-catenin
681 signaling acts upstream of N-myc, BMP4, and FGF signaling to regulate
682 proximal-distal patterning in the lung. Dev Biol. 2005;283: 226–239.
683 doi:10.1016/j.ydbio.2005.04.014
684 33. Goss AM, Tian Y, Tsukiyama T, Cohen ED, Zhou D, Lu MM, et al. Wnt2/2b
685 and β-Catenin Signaling Are Necessary and Sufficient to Specify Lung
686 Progenitors in the Foregut. Dev Cell. 2009;17: 290–298.
687 doi:10.1016/j.devcel.2009.06.005
688 34. Hrycaj SM, Dye BR, Baker NC, Larsen BM, Burke AC, Spence JR, et al. Hox5
689 genes regulate the Wnt2/2b-Bmp4-signaling axis during lung development. Cell
690 Rep. 2015;12: 903–912. doi:10.1016/j.celrep.2015.07.020
691 35. Lüdtke TH, Rudat C, Wojahn I, Weiss AC, Kleppa MJ, Kurz J, et al. Tbx2 and
692 Tbx3 Act Downstream of Shh to Maintain Canonical Wnt Signaling during
693 Branching Morphogenesis of the Murine Lung. Dev Cell. 2016;39: 239–253.
694 doi:10.1016/j.devcel.2016.08.007
695 36. Fumoto K, Takigawa-Imamura H, Sumiyama K, Kaneiwa T, Kikuchi A.
696 Modulation of apical constriction by Wnt signaling is required for lung epithelial
697 shape transition. Dev. 2017;144: 151–162. doi:10.1242/dev.141325
698 37. Kadzik RS, Cohen ED, Morley MP, Stewart KM, Lu MM, Morrisey EE. Wnt
699 ligand/Frizzled 2 receptor signaling regulates tube shape and branch-point
700 formation in the lung through control of epithelial cell shape. Proc Natl Acad Sci
701 U S A. 2014;111: 12444–12449. doi:10.1073/pnas.1406639111
702 38. Kamioka Y, Sumiyama K, Mizuno R, Sakai Y, Hirata E, Kiyokawa E, et al. Live
703 imaging of protein kinase activities in transgenic mice expressing FRET
704 biosensors. Cell Struct Funct. 2012;37: 65–73. doi:10.1247/csf.11045
705 39. Hama H, Kurokawa H, Kawano H, Ando R, Shimogori T, Noda H, et al. Scale:
706 A chemical approach for fluorescence imaging and reconstruction of transparent
707 mouse brain. Nat Neurosci. 2011;14: 1481–1488. doi:10.1038/nn.2928

40. Takigawa-Imamura H, Morita R, Iwaki T, Tsuji T, Yoshikawa K. Tooth germ invagination from cell-cell interaction: Working hypothesis on mechanical instability. J Theor Biol. 2015;382: 284–291. doi:10.1016/j.jtbi.2015.07.006
41. Gunji S, Oda Y, Takigawa-Imamura H, Tsukaya H, Ferjani A. Excess pyrophosphate restrains pavement cell morphogenesis and alters organ flatness in Arabidopsis thaliana. Front Plant Sci. 2020;11. doi:10.3389/fpls.2020.00031
42. Higaki T, Takigawa-Imamura H, Akita K, Kutsuna N, Kobayashi R, Hasezawa S, et al. Exogenous cellulase switches cell interdigitation to cell elongation in an RIC1-dependent manner in Arabidopsis thaliana cotyledon pavement cells. Plant Cell Physiol. 2017;58: 106–119. doi:10.1093/pcp/pcw183
43. Hirano T, Konno H, Takeda S, Dolan L, Kato M, Aoyama T, et al. PtdIns(3,5)P2 mediates root hair shank hardening in Arabidopsis. Nature Plants. 2018. pp. 888–897. doi:10.1038/s41477-018-0277-8
44. Hirano T, Ebine K, Ueda T, Higaki T, Watanabe-Nakayama T, Konno H, et al. The SYP123-VAMP727 SNARE complex delivers secondary cell wall components for root hair shank hardening in Arabidopsis. Plant Cell. 2023;35: 4347–4365. doi:10.1093/plcell/koad240
45. Fumoto K, Takigawa-Imamura H, Sumiyama K, Yoshimura SH, Maehara N, Kikuchi A. Mark1 regulates distal airspace expansion through type I pneumocyte flattening in lung development. J Cell Sci. 2019;132. doi:10.1242/jcs.235556
46. Hirashima T, Iwasa Y, Morishita Y. Mechanisms for split localization of Fgf10 expression in early lung development. Dev Dyn. 2009;238: 2813–2822. doi:10.1002/dvdy.22108
47. Francavilla C, Rigbolt KTG, Emdal KB, Carraro G, Vernet E, Bekker-Jensen DB, et al. Functional Proteomics Defines the Molecular Switch Underlying FGF Receptor Trafficking and Cellular Outputs. Mol Cell. 2013;51: 707–722. doi:10.1016/j.molcel.2013.08.002
48. Warburton D, Bellusci S, De Langhe S, Del Moral PM, Fleury V, Mailleux A, et al. Molecular Mechanisms of Early Lung Specification and Branching Morphogenesis. Pediatr Res. 2005;57: 26R-37R. doi:10.1203/01.PDR.0000159570.01327.ED
49. Bar-ziv R, Moses E. Instability and “pearling” states produced in tubular membranes by competition of curvature and tension. Phys Rev Lett. 1994;73:

741 1392–1395.
742 50. De Langhe SP, Sala FG, Del Moral PM, Fairbanks TJ, Yamada KM, Warburton
743 D, et al. Dickkopf-1 (DKK1) reveals that fibronectin is a major target of Wnt
744 signaling in branching morphogenesis of the mouse embryonic lung. Dev Biol.
745 2005;277: 316–331. doi:10.1016/j.ydbio.2004.09.023
746 51. Yin Y, White AC, Huh SH, Hilton MJ, Kanazawa H, Long F, et al. An FGF-
747 WNT gene regulatory network controls lung mesenchyme development. Dev
748 Biol. 2008;319: 426–436. doi:10.1016/j.ydbio.2008.04.009
749 52. Volckaert T, Campbell A, Dill E, Li C, Minoo P, De Langhe S. Localized Fgf10
750 expression is not required for lung branching morphogenesis but prevents
751 differentiation of epithelial progenitors. Dev. 2013;140: 3731–3742.
752 doi:10.1242/dev.096560
753 53. Soleas JP, D'Arcangelo E, Huang L, Karoubi G, Nostro MC, McGuigan AP, et
754 al. Assembly of lung progenitors into developmentally-inspired geometry drives
755 differentiation via cellular tension. Biomaterials. 2020;254: 120128.
756 doi:10.1016/j.biomaterials.2020.120128
757

FIG 1

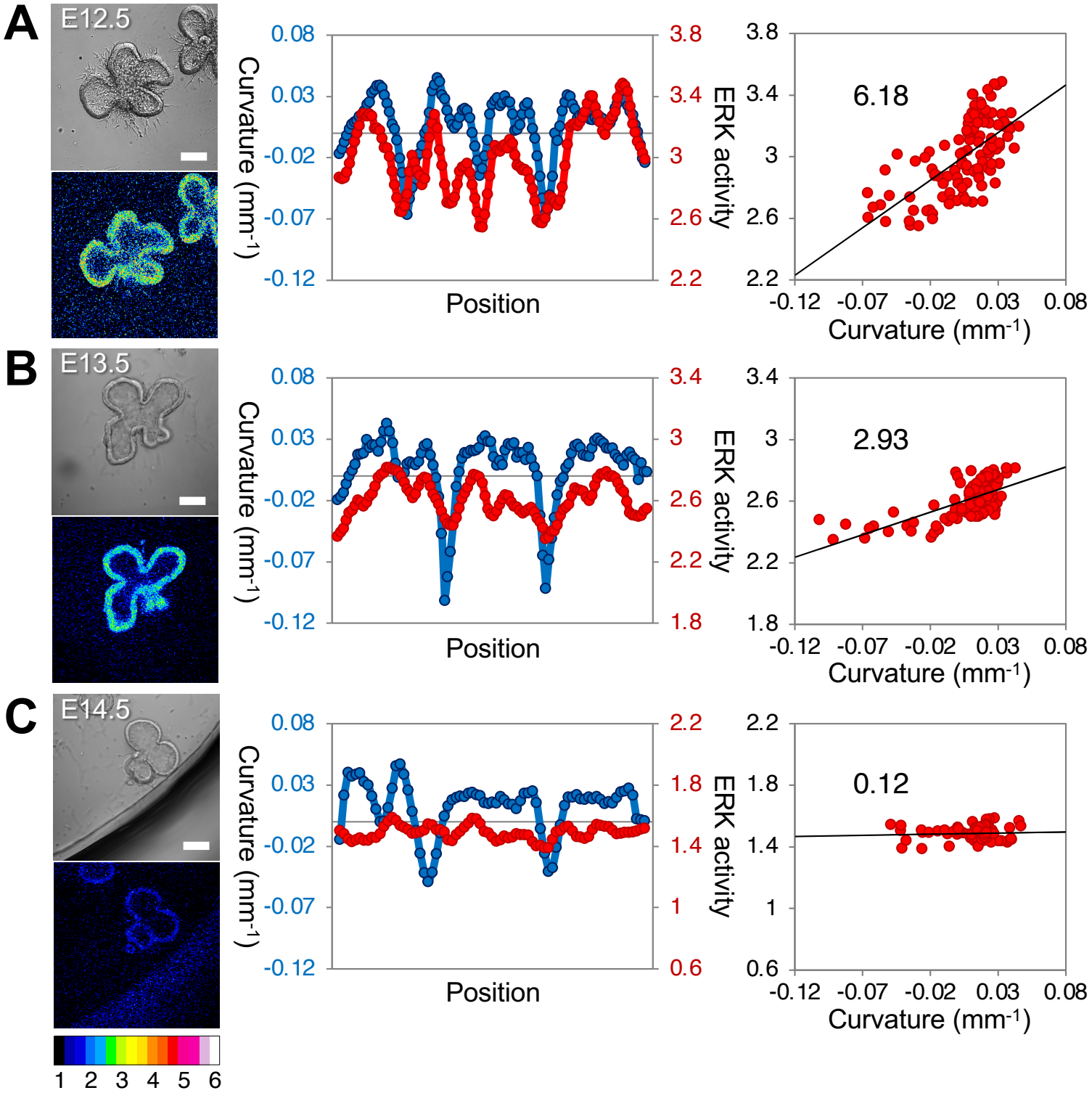
A
E12.5
B
E13.5
C
E14.5
Curvature (mm-1)
ERK activity
Position
Curvature (mm-1)
6.18
2.93
0.12
1 2 3 4 5 6

FIG 2

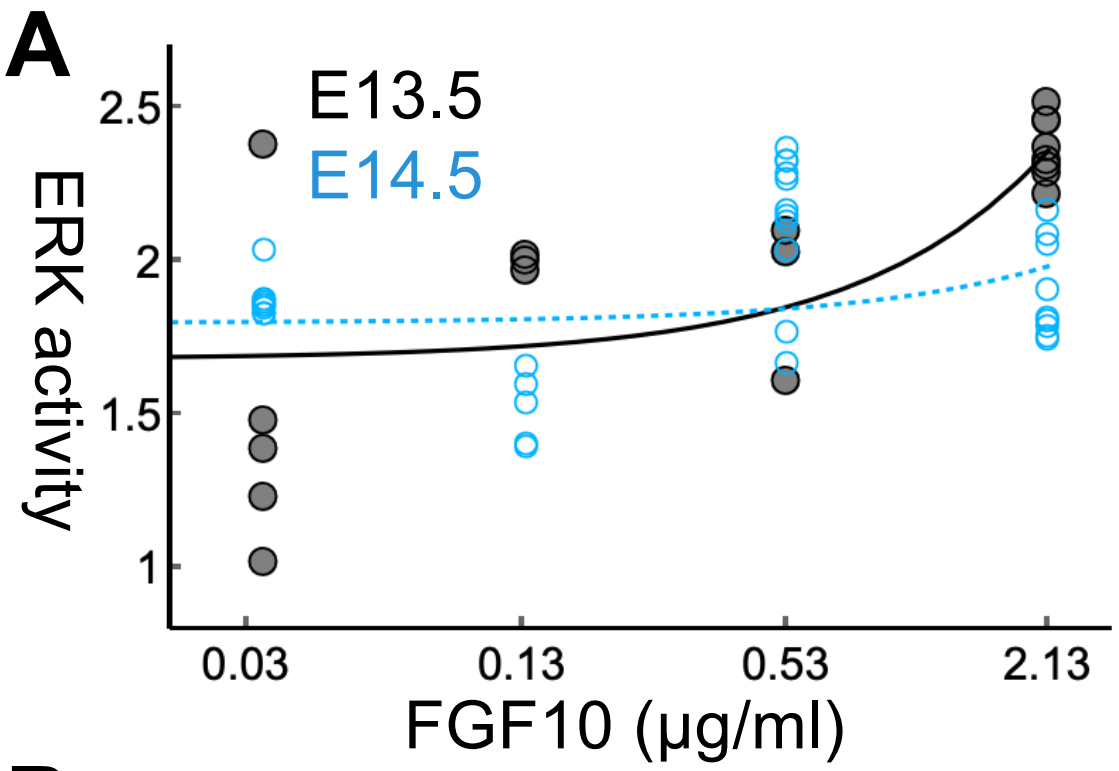
A
E13.5
E14.5
ERK activity
2.5
2
1.5
1
0.03
0.13
0.53
2.13
FGF10 (μg/ml)

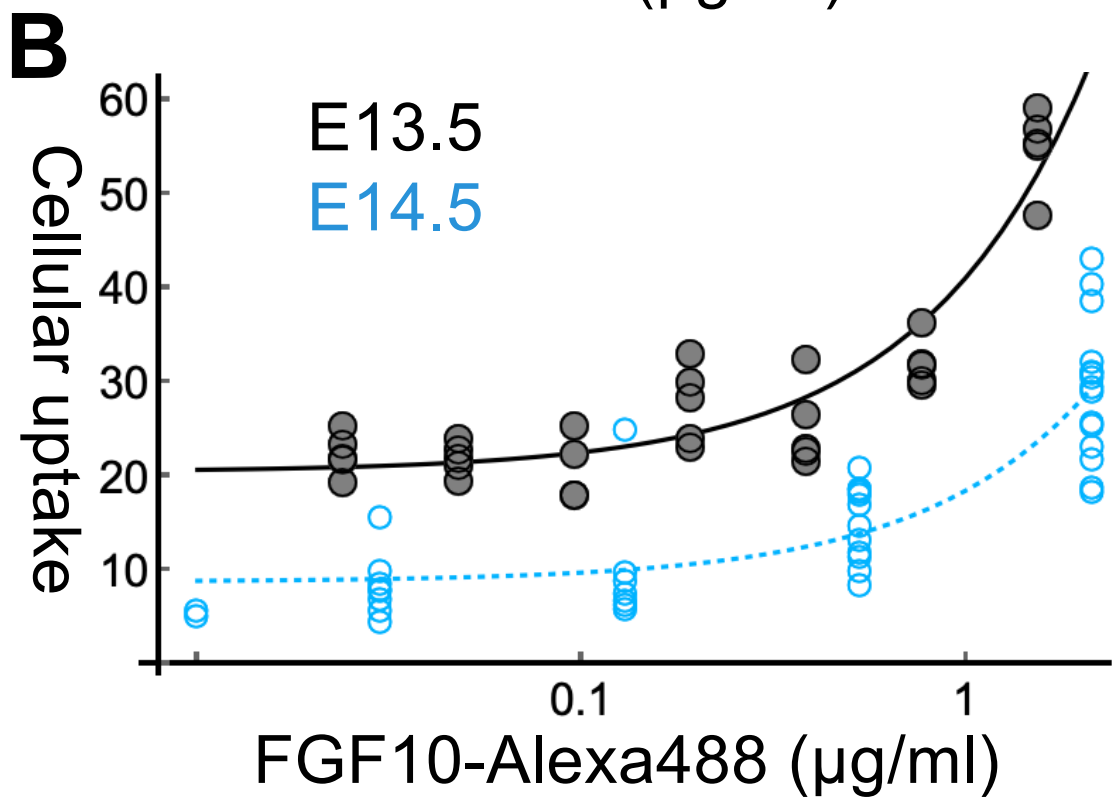
B
E13.5
E14.5
Cellular uptake
60
50
40
30
20
10
0.1
1
FGF10-Alexa488 (μg/ml)

FIG 3

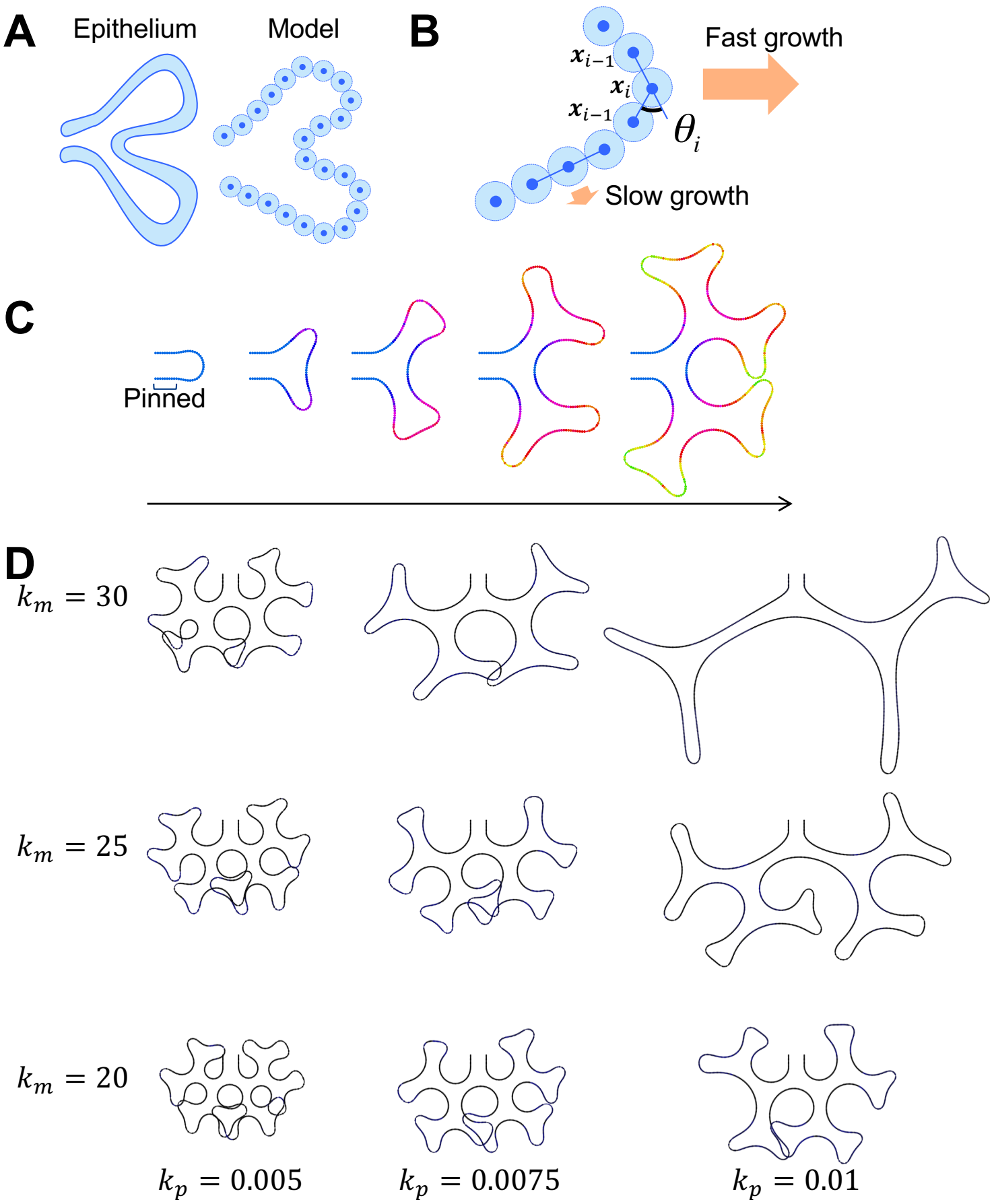
A
Epithelium
Model
B
x_{i-1}
x_i
x_{i-1}
θ_i
Fast growth
Slow growth
C
Pinned
D
$k_m = 30$
$k_m = 25$
$k_m = 20$
$k_p = 0.005$
$k_p = 0.0075$
$k_p = 0.01$

FIG 4

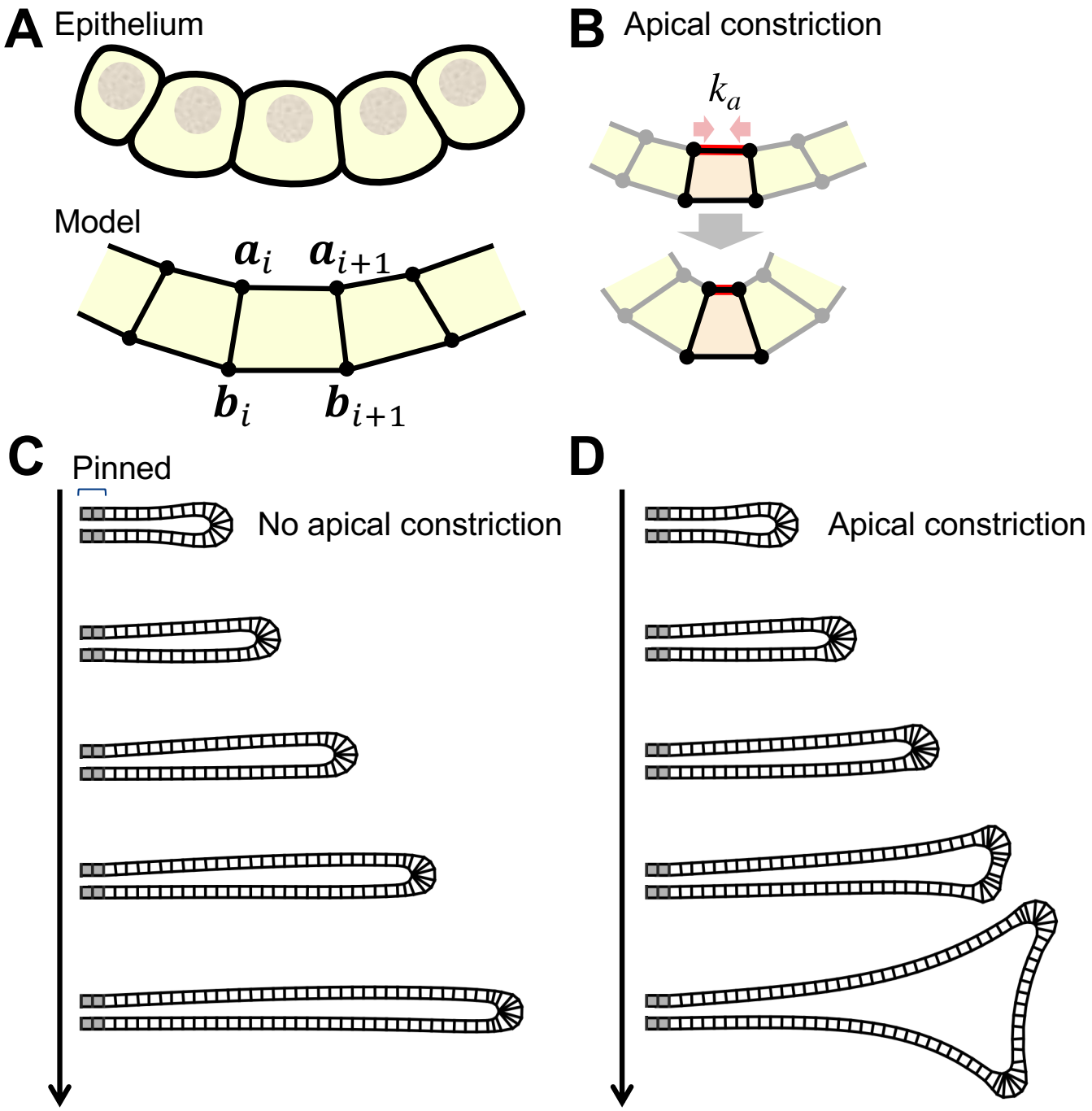
A
Epithelium
Model
a_i
a_{i+1}
b_i
b_{i+1}
B
Apical constriction
k_a
C
Pinned
No apical constriction
D
Apical constriction

FIG 5

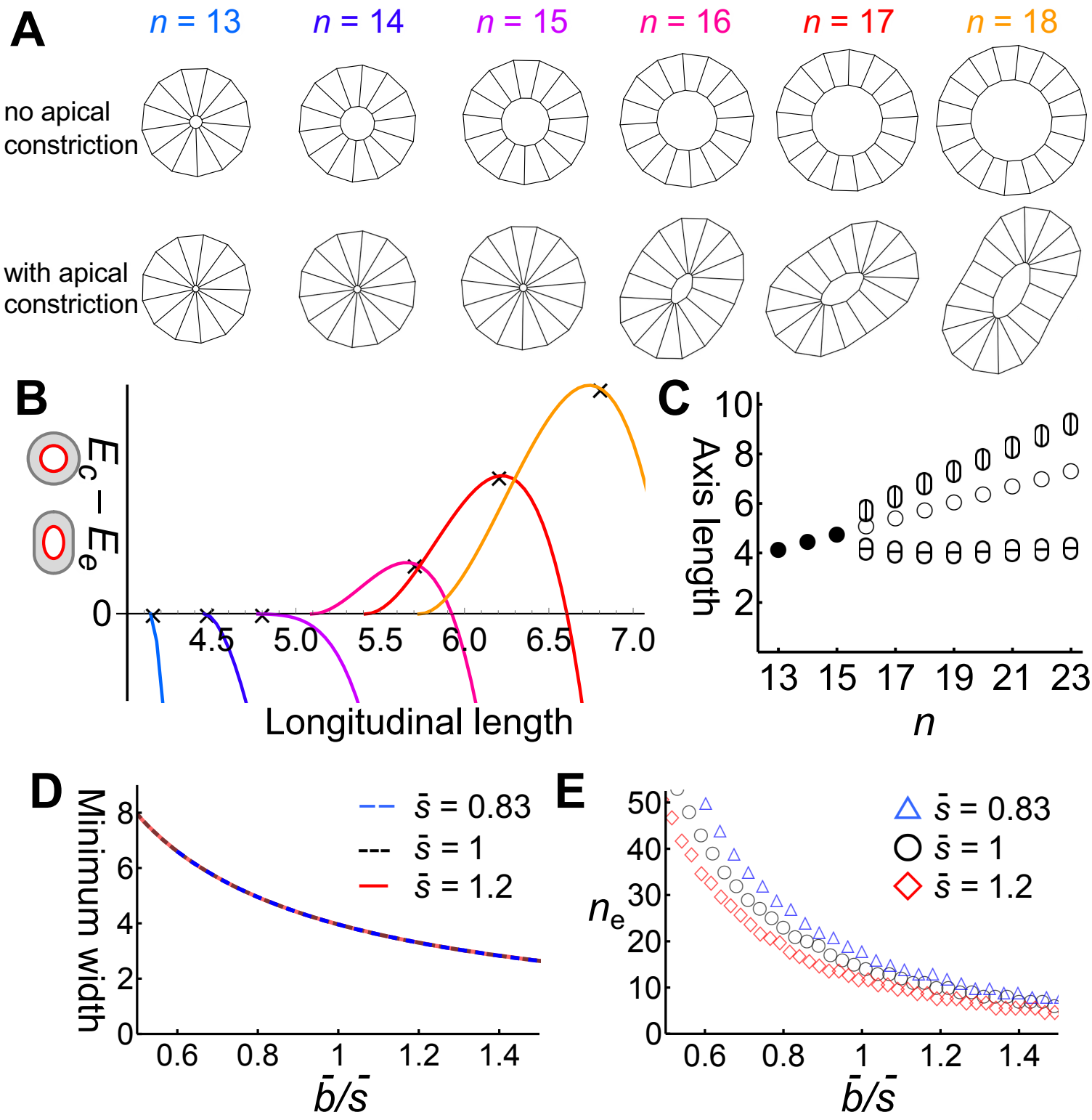
A
n = 13
n = 14
n = 15
n = 16
n = 17
n = 18
no apical constriction
with apical constriction
B
$E_c - E_e$
0
4.5
5.0
5.5
6.0
6.5
7.0
Longitudinal length
C
Axis length
10
8
6
4
2
13
15
17
19
21
23
n
D
Minimum width
8
6
4
2
0
0.6
0.8
1
1.2
1.4
$\bar{b}/\bar{s}$
$\bar{s}$ = 0.83
$\bar{s}$ = 1
$\bar{s}$ = 1.2
E
n_e
50
40
30
20
10
0
0.6
0.8
1
1.2
1.4
$\bar{b}/\bar{s}$
$\bar{s}$ = 0.83
$\bar{s}$ = 1
$\bar{s}$ = 1.2

FIG 6

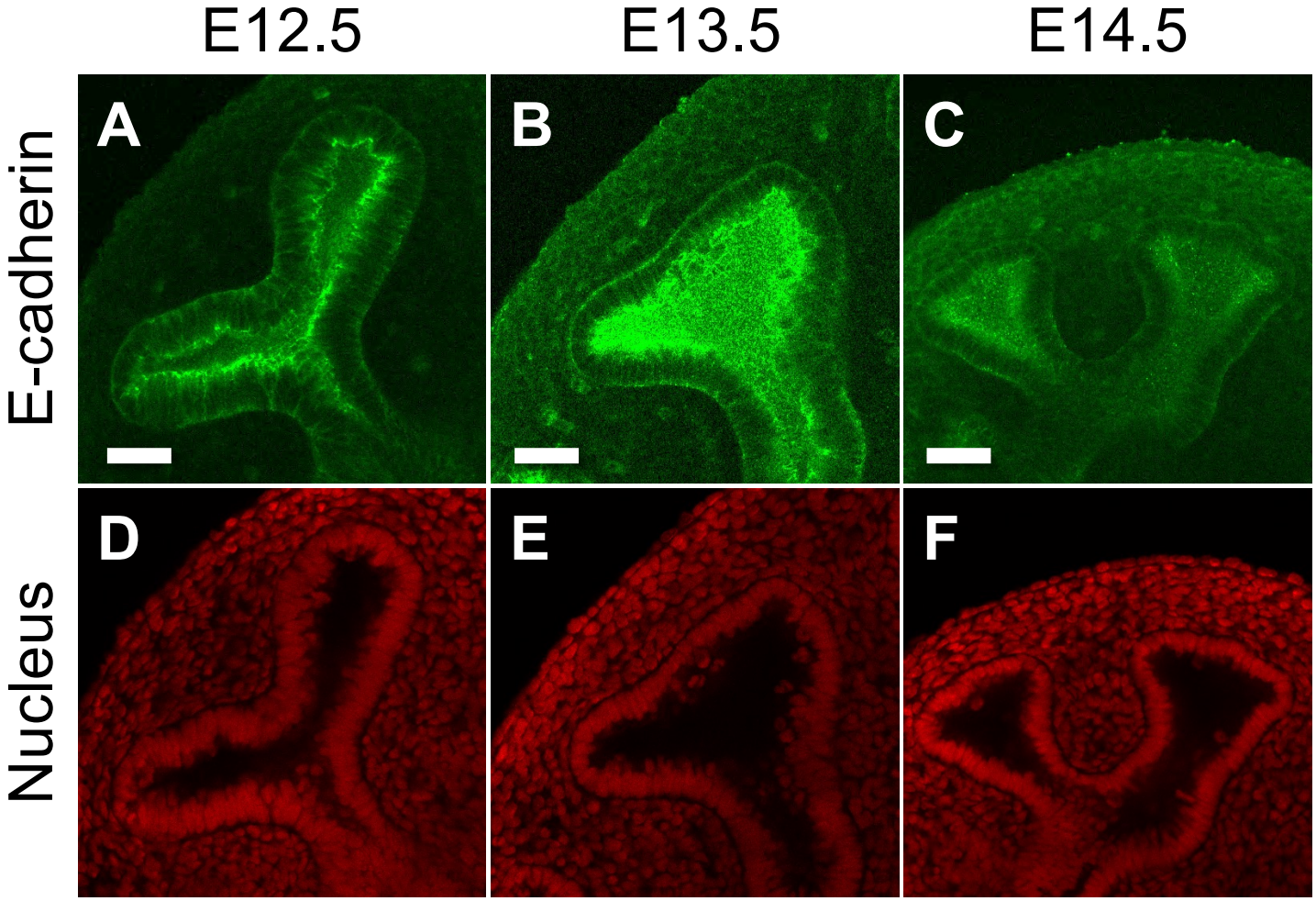

FIG 7

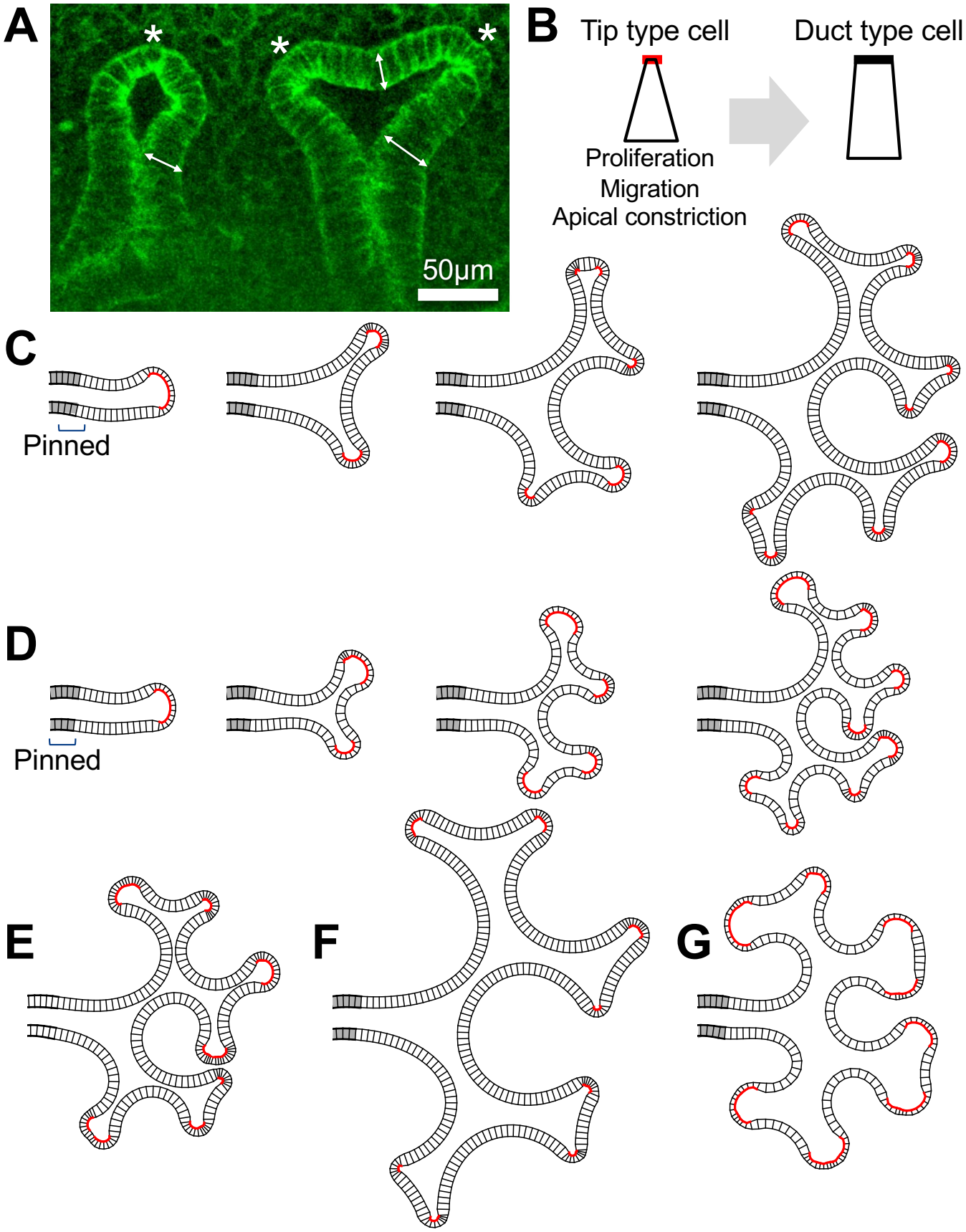
A
50μm
B
Tip type cell
Duct type cell
Proliferation
Migration
Apical constriction
C
Pinned
D
Pinned
E
F
G

Figure Legend

Fig 1

Map of ERK activity in embryonic mouse lungs. The upper left panel is the bright-field image, and the lower left panel shows the heat map representation of ERK activity. The middle panel shows cross-sectional tissue curvature (blue, left axis) and ERK activity (red, right axis) along the epithelial section. The right panel shows the correlation between the curvature and ERK activity. The color bar indicates the range of ERK activity. Epithelium explants at E12.5 **(A)**, E13.5 **(B)**, and E14.5 **(C)** were cultured with 500 ng/mL FGF10 for 18 h. The values in the figure represent the slope of the signal to curvature, determined through linear regression analysis (R^2 = 0.41 at E12.5, R^2 = 0.45 at E13.5, R^2 = 0.0031 at E14.5). Scale bars: 100 μm.

Fig 2

FGF10 dose dependency of the cellular response in E13.5 (black) and E14.5 (blue) epithelium. (**A**) The ERK activity of each cyst is represented by a dot in the semilog plot. The lung epithelium cysts of E13.5 and E14.5 (19 and 34 cysts, respectively) were cultured with FGF10 at concentrations of 0.03, 0.13, 0.53, and 2.13 μg/mL for 18 h. Linear regression analysis showed $y = 0.330x + 1.68$ with R^2 = 0.53 for E13.5 and $y = 0.0334x + 1.89$ with R^2 = 0.012 for E14.5. (**B**) The cellular uptake of FGF10-Alexa488 for 3 h was estimated for 34 and 44 explants of E13.5 and E14.5 lung, respectively. Each dot in the semilog plot represents a mean fluorescent intensity in an epithelial area of a cross-section. The concentration of

780 FGF10-Alexa488 was 0.024, 0.048, 0.097, 0.19, 0.38, 0.78, and 1.55 for E13.5, and
781 0.03, 0.13, 0.53, and 2.13 μg/mL for E14.5. Linear regression analysis showed $y =$
782 $20.7x + 20.4$ with $R^2 = 0.87$ for E13.5, and $y = 9.75x + 8.80$ with $R^2 = 0.72$ for E14.5.

783 **Fig 3**

784 Protrusion growth described by the particle cell model. **(A)** The epithelial cell
785 was represented by the particle in the model. The cell-cell distance is denoted by d.
786 **(B)** Cell division was described by replacing a particle with two small particles,
787 which gradually grow to the prescribed size. **(C)** The process of higher-order
788 branching. Snapshots at $t = 0$, 75, 150, 225, and 300 are shown. The proximal end
789 was pinned, and the distal tip was growing. The color indicates the cell generation.
790 The number of cells was initially 50 and was increased to 450. **(D)** Branch scale
791 control by curvature-dependent growth. Calculations corresponding to (C) were
792 performed until the number of cells reached 800.

793 **Fig 4**

794 Effect of apical constriction on branch shape shown using the quadrilateral cell
795 model. **(A)** The cross-section of epithelium is described as a sequence of
796 quadrilaterals. The i-th cell was defined by four vertices $\boldsymbol{a}_i$, $\boldsymbol{a}_{i+1}$, $\boldsymbol{b}_i$, and $\boldsymbol{b}_{i+1}$. **(B)**
797 Apical constriction is described by the attraction between apical vertices, with its
798 strength represented by k_a. **(C)** Curvature-dependent growth process. Snapshots at
799 timesteps $t = 0$, 750 1750, 2750, and 3750 are shown. Pinned cells are indicated in
800 gray. The case without apical constriction $k_a = 0$ is shown. **(D)** Apical constriction
801 was introduced with $k_a = 1$.

802 **Fig 5**

803 Mechanical instability of small cysts by apical constriction in the quadrilateral
804 cell model. **(A)** Cyst of n cells was relaxed for a sufficient time (upper panels), then
805 apical constriction was introduced and deformation was observed (lower panels).
806 **(B)** The potential energy difference between the circular state (E_c) and the elongated
807 state (E_e). Color corresponds to the cyst sizes in (A). The vertical axis is the
808 longitudinal cyst length L. The minimum L corresponds to the diameter in the
809 circular state. The cross indicates the cyst length under apical constriction in the
810 numerical simulation (A), indicating that the energy calculation predicted the model
811 behavior. **(C)** Estimated stable cyst shapes obtained from energy calculations plotted
812 along the cell number n. When $n \leq 15$, the stable shape was circular (closed circle).
813 When $n \geq 16$, the cyst was elongated, and the longitudinal length (ellipse with a
814 vertical line) and the width (ellipse with a horizontal line) were plotted. The diameter
815 of the corresponding circular cyst for $n \geq 16$ was plotted for reference (open circle).
816 **(D)** Estimated minimum cyst width for $13 \leq n \leq 27$. The vertical axis represents $\bar{b}/\bar{s}$,
817 where $\bar{b}$ is the cellular basal length and $\bar{s}$ is the cellular area. Colors represent s
818 values: 0.83 (blue dashed line), 1 (black dotted line), and 1.2 (red line). **(E)**
819 Estimated critical cell number n_e for the shape transition from circular to elongated.

820 **Fig 6**

821 Changes in epithelial thickness during lung development. **(A–C)** E-cadherin
822 staining was performed to show the epithelial shape of the growing tip at E12.5 (A),
823 E13.5 (B), and E14.5 (C). **(D–F)** Corresponding nuclear staining with PI is presented.
824 Scale bar: 100 μm.

Fig 7

Cell type switching model. **(A)** The growing tip of E14.5 mouse lung. Arrows indicate tall cells at concave regions and asterisks indicate short cells. **(B)** Two cell types in the model. Tip type cells exhibit proliferation, outward migration, and apical constriction (left). Duct type cells are tall and do not show these activities (right). The switch from the tip type to the duct type occurs based on a decrease in local curvature. **(C)** Snapshots of the growing process in the case of thick epithelium with high curvature dependency. The gray color represents cells pinned at their initial positions. The red color on the apical side represents tip type cells. **(D)** Thin epithelium with low curvature dependency. **(E)** Thick epithelium with low curvature dependency, showing the intermediate morphology between (C) and (D). **(F and G)** The cases of low apical constriction activity. Thick epithelium with high curvature dependency (F) and thin epithelium with low curvature dependency (G) are shown.